Molecular Dynamics Simulation of Deoxy and Carboxy Murine Neuroglobin in Water

Massimiliano Anselmi,* Maurizio Brunori,† Beatrice Vallone,† and Alfredo Di Nola*
*Dipartimento di Chimica and †Dipartimento di Scienze Biochimiche, Università di Roma "La Sapienza", Rome, Italy

ABSTRACT Globins are respiratory proteins that reversibly bind dioxygen and other small ligands at the iron of a heme prosthetic group. Hemoglobin and myoglobin are the most prominent members of this protein family. Unexpectedly a few years ago a new member was discovered and called neuroglobin (Ngb), being predominantly expressed in the brain. Ngb is a single polypeptide of 151 amino acids and despite the small sequence similarity with other globins, it displays the typical globin fold. Oxygen, nitric oxide, or carbon monoxide can displace the distal histidine which, in ferrous Ngb as well as in ferric Ngb, is bound to the iron, yielding a reversible adduct. Recent crystallographic data on carboxy Ngb show that binding of an exogenous ligand is associated to structural changes involving heme sliding and a topological reorganization of the internal cavities; in particular, the huge internal tunnel that connects the bulk with the active site, peculiar to Ngb, is heavily reorganized. We report the results of extended (90 ns) molecular dynamics simulations in water of ferrous deoxy and carboxy murine neuroglobin, which are both coordinated on the distal site, in the latter case by CO and in the former one by the distal His^{64}(E7). The long timescale of the simulations allowed us to characterize the equilibrated protein dynamics and to compare protein structure and dynamical behavior coupled to the binding of an exogenous ligand. We have characterized the heme sliding motion, the topological reorganization of the internal cavities, the dynamics of the distal histidine, and particularly the conformational change of the CD loop, whose flexibility depends ligand binding.

INTRODUCTION

Globins are water-soluble respiratory proteins that reversibly bind dioxygen and other small ligands at the iron of a heme prosthetic group that is buried in a highly conserved α-helical globin fold. Hemoglobin (Hb) and myoglobin (Mb) are the most prominent members of this protein family (1). In 2000, neuroglobin (Ngb), a new member of the vertebrate globin family, was discovered (2).

Ngb, a single polypeptide of 151 amino acids, is expressed in the nervous tissues. Despite the small sequence similarity to the other globins (<25% of sequence), Ngb conserves a number of canonical residues: among others, a proximal histidine His^{96}(F8) that binds to the heme iron, and a distal histidine His^{64}(E7) facing the binding site of O_2 and other diatomic ligands (3,4). However, in contrast to Mb and Hb, in the absence of exogenous ligands both the ferric and the ferrous forms of Ngb are hexacoordinated to the distal and the proximal His residues (5,6); in the absence of an exogenous ligand, they are conventionally referred to as unliganded states. In the presence of ligand binding with O_2 and CO, only the ferrous form is observed.

Binding of O_2, CO, and NO to the ferrous heme iron displaces His^{64}(E7), to yield a reversible adduct. This reaction implies a competition between the exogenous ligand and the endogenous His^{64}(E7), the rupture of the sixth coordination bond being a prerequisite for binding. The kinetics of this process has been studied by stopped-flow and by laser photolysis of the adducts of reduced Ngb with O_2, CO, and NO (5–11). Rapid mixing kinetic data showed that binding of an exogenous ligand to reduced deoxy Ngb is slow ($t_{1/2}$ = ~1 s) and ligand concentration independent, as expected. The three-dimensional structure has been solved by x-ray crystallography for the unliganded ferric Ngb from man and mouse (3,4) and for the CO-bound ferrous form (12). The latter article showed that binding of CO is associated to structural changes involving a significant heme sliding and a topological reorganization of the internal cavities; in particular, the huge internal tunnel connecting the bulk to the active site (a peculiarity of Ngb) is topologically reorganized.

The physiological role of Ngb is not well understood. Average Ngb concentration seems too low (<1 μM) to play a Mb-like role in transport or storage of O_2, although this function is not yet excluded. A remarkable neuroprotective role of Ngb has been convincingly demonstrated, since upregulation of Ngb expression was observed under hypoxia or ischemia in vitro and in vivo; more important, neuronal survival after hypoxia was impaired by inhibiting Ngb expression and enhanced by overexpression (13,14). Therefore, Ngb is involved in activating a neuroprotective mechanism of response to hypoxia and ischemia in the brain, and plays a role in the recovery from stroke (14). However, the biochemical mechanism involved is still a conundrum.

Molecular dynamics (MD) simulations have provided important insight into the structure and function of globins such as Mb and Hb (15–20). Recently, extended MD simulations allowed us to follow the CO migration in the interior of myoglobin, as well as the effects of mutations and trapped

Submitted October 17, 2006, and accepted for publication March 26, 2007.
Address reprint requests to A. Di Nola, Tel.: 39-06-4991-3122; E-mail: dinola@caspur.it.
Editor: Ron Elber.

0006-3495/07/07/434/08 $2.00
doi: 10.1529/biophysj.106.099648

CO on the Mb structure and cavities dynamics (21,22), in correlation with experimental studies (23–25).

This article reports the results of extended (90 ns) MD simulations of deoxy and carboxy murine Ngb in water. The purpose is to compare the structural dynamics of deoxy and carboxy Ngb in solution, in particular the heme group motion and the related internal cavities fluctuations that appear so peculiar compared to other globins. To this end, the same oxidation state has been chosen. Starting from the crystallographic coordinates (12), our MD results show a large amplitude motion of the heme in NgbCO and a corresponding large fluctuation of the cavities. In addition, we have documented a flip/flop motion of the CD loop upon CO binding, which is correlated to the His^{64}(E7) configuration and seems to be particularly significant to evaluate the possible role of Ngb as a molecular signal transducer involved in neuroprotection (26,27).

METHODS

The starting coordinates employed for the simulations were taken from the x-ray structure of CO-bound ferrous murine Ngb at 1.7 Å resolution (PDB entry 1w92) (12); in the case of deoxy Ngb, we used the 1.5 Å resolution structure of murine ferric bis-histidine Ngb (PDB entry 1q1f) (4). The crystallographic structures were obtained with a Ngb mutant (C55S/C120S), since the presence of oxidizable cysteines in the wild-type protein hindered crystallization. Murine ferric Ngb shows the presence of two different protein conformers (relative occupancy ~70:30) due to heterogeneity of the heme group orientation, for a 180° rotation around the α-γ meso axis (4,28); also the proximal His^{96}(F8) and the distal His^{64}(E7) histidines assume two conformations, with the same ratio of occupancy. In the deoxy Ngb simulation, we have used the crystal structure of the conformer with the major occupancy and simply assigned the ferrous oxidation state to the metal.

To determine the partial charges of the hexacoordinated heme in deoxy and carboxy Ngb, we performed the quantum chemical calculations on the isolated bis(imidazole) $iron^{II}$ porphyrin [$Fe^{II}P(Im)_2$] complex and the carboxy-imidazole $iron^{II}$ porphyrin [$Fe^{II}P(CO)(Im)$] complex, respectively. Density functional calculations, Becke's three parameters exchange (29), and Lee, Yang, Parr correlation (B3LYP) (30) were performed. All our quantum chemical calculations were carried out using the GAMESS US package (31). In the GROMOS force field, the heme iron neighbor has been defined through a single charge group with the following partial atomic charges: 0.4 *e* for the iron and −0.1 *e* for the four pyrrolic nitrogen atoms. Therefore, we have chosen to change only the iron charge group. We used the Ahlrichs VTZ basis set (32) for the iron and the 6-311+G* basis set for the nitrogen atoms of the heme and the heteroatoms of the imidazole and carbon monoxide molecules. We have used the 3-21G basis set for the rest of the system and for all hydrogen atoms. The partial charges have been obtained from the CHELPG algorithm, and the fitted charges have been constrained to exactly reproduce the total charge and the calculated dipole moment of the system. In conclusion we have chosen the following set of partial charges: for deoxy Ngb, 0.3 *e* for the iron and −0.075 *e* for the pyrrolic nitrogen atoms, while for carboxy Ngb, 0.6 *e* for the iron and −0.15 *e* for the heme nitrogen atoms; for the CO bound to the hexacoordinated ferrous heme, we have used 0.17 *e* for the carbon and −0.17 *e* for the oxygen atom.

Each protein was solvated in a box with explicit single-point charge water molecules (33), large enough to contain the protein and 0.8 nm of solvent on all sides. The total number of atoms for the systems was ~21,000.

MD simulations were performed with the GROMACS software package (34) using GROMOS96 force field (35). The additional parameters for hexacoordinated heme and bound CO were taken from the GROMOS force-field parameter sets 53A6 (36). Simulations were carried out at constant temperature of 300 K within a fixed-volume rectangular box using periodic boundary conditions. The LINCS algorithm (37) to constrain bond lengths and the rototranslational constraint algorithm (38) were used. The initial velocities were taken randomly from a Maxwellian distribution at 300 K and the temperature was held constant by the isothermal algorithm (39). By using dummy hydrogen atoms (40), a time step of 4 fs could be chosen; we have also redistributed the water oxygen mass on the hydrogen atoms to improve the stability of the simulations. The particle mesh Ewald method (41) was used for the calculation of the long-range interactions with a grid spacing of 0.12 nm combined with a fourth-order B-spline interpolation to compute the potential and forces in between grid points. A nonbond pair list cutoff of 9.0 Å was used and the pair list was updated every four time steps. For all systems, the solvent was relaxed by energy minimization followed by 100 ps of MD at 300 K, while restraining protein atomic positions with a harmonic potential. The systems were then minimized without restraints and their temperature brought to 300 K in a stepwise manner: 50 ps MD runs were carried out at 50, 100, 150, 200, 250, and 300 K, before starting the production runs at 300 K.

We used the essential dynamics technique (42) to characterize the dynamical behavior of the protein.

The package SURFNET (43) was used for detecting the cavities and calculating their volumes. In this program, gap regions are defined by filling the empty regions in the interior of the molecule with gap spheres of variable radius (R_{min} = 1.0 Å and R_{max} = 3.0 Å, in our case). These spheres are then used to compute a three-dimensional density map that, when contoured, defines the surface of the gap region. Cavity volumes were evaluated without taking into account the presence of the water and of CO in the case of carboxy Ngb simulation. A cavity is considered exposed if the SURFNET program shows a continuity between the cavity and the solvent.

RESULTS

The root mean-square deviation of C_α atoms (data not shown), obtained from deoxy and carboxy Ngb (NgbCO) simulations with respect to their crystallographic structures, shows that within 15 ns the two trajectories reach values of ~1.8 Å and ~2.4 Å, for the deoxy Ngb and NgbCO respectively; a small drift is then observed up to 90 ns. The residue-based root mean-square fluctuation for C_α (data not reported) shows that the main root mean-square fluctuation difference between deoxy and NgbCO is located around the residue Glu^{80}, in the EF loop. The drastic reduction of the EF loop fluctuation in NgbCO with respect to deoxy is in agreement with the x-ray diffraction data (12).

The motion of the heme in the NgbCO simulation was monitored with the essential dynamics analysis, which was performed on all the heme atoms (with the exception of the terminal propionic chains). The eigenvectors with large eigenvalues correspond to the principal directions of motion of the heme group. The motion associated to the first eigenvector (Fig. 1 *A*) is revealed to be, essentially, a rototranslational displacement in the direction from D to B pyrrole rings (Fig. 2): the two extreme heme configurations onto the first essential eigenvector correspond to a total displacement of ~1.85 Å for the heme iron. The rotation around an axis parallel to the macrocycle average plane, centered in the iron atom and in the direction connecting the A and C pyrrole rings, is ~9° for the two extreme configurations. This

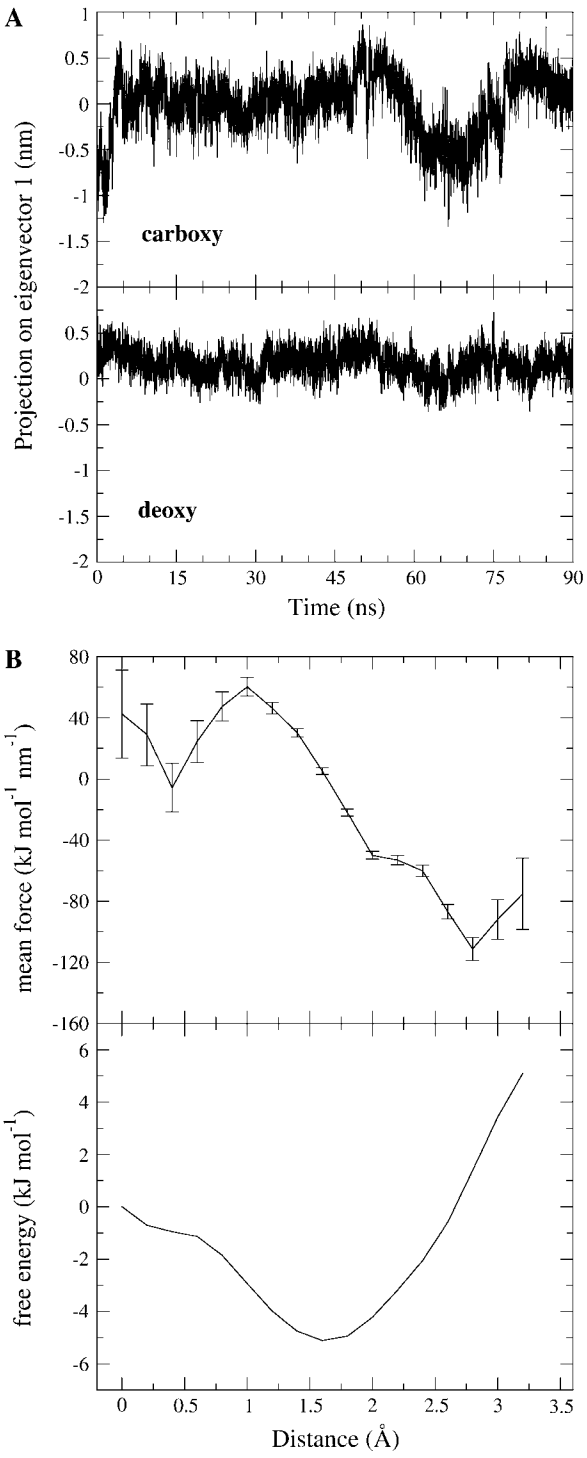

FIGURE 1 (*A*) Trajectory of the heme displacement along its first essential eigenvector in carboxy Ngb (*upper panel*) and deoxy Ngb (*lower panel*). The position of the heme in the crystal structure of carboxy Ngb (*upper panel*) corresponds to the negative (~ -0.5) values at $t = 0$ and $t = \sim 65$ ns. In the remaining part of the simulation the heme group position roughly corresponds to its position in the metNgb crystal structure. (*B*) Mean force with their standard deviations (*upper panel*) and heme group free energy landscape (*bottom panel*). Briefly, the method is based on the choice of a direction and on the calculation of the mean force acting on the heme center of mass along this direction. The mean force corresponds to the free energy gradient.

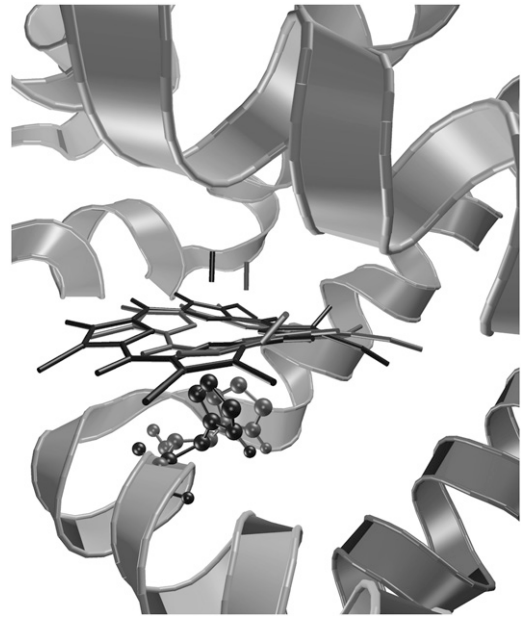

FIGURE 2 Extreme configurations assumed by the heme during the carboxy Ngb simulation, corresponding to extreme values of the projection onto the first essential eigenvector.

rototranslational motion corresponds to the heme sliding movement observed in comparing the crystal structures of NgbCO and metNgb (12). It has to be noted that the position, which corresponds to the positive value of the trajectory projection (Fig. 1 *A*), is not allowed in NgbCO crystal structure, due to close contacts between the CO bound to the heme and the distal His^{64}(E7); however, a displacement of the latter (<1 Å measured on the His^{64} side-chain center of mass) drastically reduces the atomic hindrance, although never corresponds to the different conformations identified in Mb and underlying the generally called histidine-gate mechanism (44).

The free energy landscape of the heme displacement was calculated by the use of the potential of mean force method (45), as reported in Fig. 1 *B*. The abscissa refers to a direction connecting the two extreme positions of the heme in the simulation. The free energy plot shows a minimum at 1.7 Å, a position corresponding to that seen in the metNgb crystal structure. The position of the heme in the NgbCO crystal structure ($\sim$0.3 Å in Fig. 1 *B*) corresponds to an almost flat region whose free energy value is $\sim$5 kJ/mol higher than the minimum.

In Fig. 3 (*upper panel*), the trajectory of the distal His^{64}(E7) χ_1 torsion angle is reported for both derivatives. While for deoxy Ngb the side-chain conformation of the His^{64}(E7) is blocked (*shaded line*) because of its covalent bond with the heme iron, in the NgbCO simulation (*solid line*) His^{64}(E7) is free to flip between two different conformations corresponding to two different values of χ_1 torsion angle. In Mb, identical values of the χ_1 torsion angle correspond to the opening and closure of the so-called histidine gate, although the dynamical behavior of the distal histidine

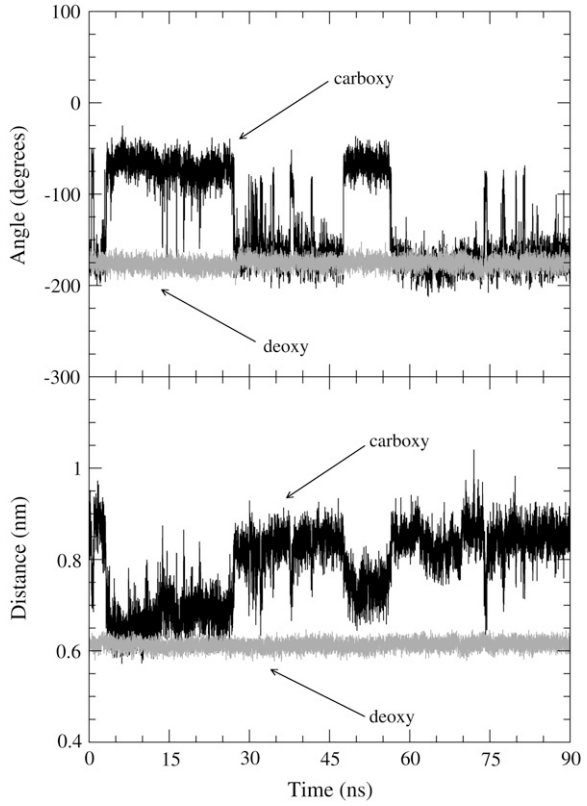

FIGURE 3 (*Upper panel*) Trajectory of the distal histidine His^{64} χ_1 torsion angle for carboxy (*solid line*) and deoxy Ngb (*shaded line*). (*Lower panel*) Trajectory of the heme iron-$His^{64}(C_\alpha)$ distance for carboxy (*solid line*) and deoxy Ngb (*shaded line*).

His^{64}(E7) neighboring residues is quite different in the two proteins; thus while in Mb the His^{64}(E7) rotation causes the opening and the closure of the so-called histidine gate (44), in Ngb it is on the other hand associated to a substantial downward displacement of helix E, as can be noted in Fig. 3 (*lower panel*) where the trajectory of the distance between the heme iron and the distal histidine C_α atom is reported. Fig. 3 also shows that the displacement of helix E is highly correlated with the distal His^{64}(E7) χ_1 torsion angle, while no correlation is observed with the heme position (Fig. 1 *A*). The C_α atom displacements toward the heme group of the residues Phe^{61}, His^{64}, Lys^{67}, and Leu^{70} of the E helix are 1.7 Å, 1.3 Å, 0.9 Å, and 1.0 Å, respectively, corresponding to a rototranslational motion of this helix.

Although no opening of the so-called histidine gate is observed in Ngb, we will refer the two states of the χ_1 torsion angle as open and closed. The configuration of the His^{64}(E7) χ_1 torsion angle is also correlated to the configuration of the CD corner, composed by the α-helices C and D and the CD loop. In fact, when the His^{64}(E7) is in the open configuration, the CD loop flips between the two configurations reported in Fig. 4. It has to be noted that in the crystal structure the distance between the His^{64}(E7) C_α and the center of the CD loop, represented by the Asn^{45} C_α, is 14.3 Å and that the maximum displacement of the Asn^{45} C_α in the simulation is ~5 Å. The dynamical behavior of the CD corner has been studied by the essential dynamics analysis. In Fig. 5, we

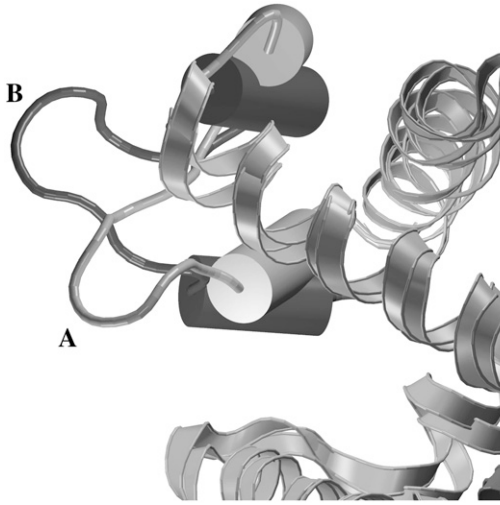

FIGURE 4 Extreme configurations assumed by the CD corner (*A* and *B*) during simulation, corresponding to extreme values of the projection onto the first essential eigenvector.

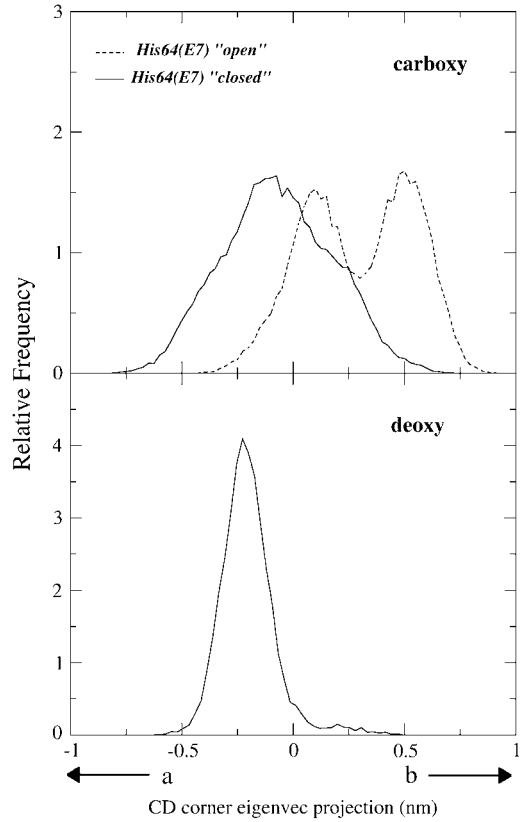

FIGURE 5 Distribution of the projection onto the CD corner first essential eigenvector, for deoxy Ngb (*lower panel*) and carboxy Ngb (*upper panel*), corresponding to the distal His^{64}(E7) closed (*solid line*) or open (*dashed line*) configuration. The lower-case letters *a* and *b* on the bottom are referred to the extreme configurations assumed by the CD corner.

report the distribution of the projection of its trajectory onto the first essential eigenvector. A bimodal distribution is observed when the His^{64}(E7) is in the open configuration and the distance between the His^{64}(E7) C_α and the heme iron is small; conversely, when the His^{64}(E7) is closed and the His^{64}-Fe distance increases, a unimodal distribution is observed. It can be concluded that the CD corner conformational state is correlated to the His^{64}(E7) configuration. As can be noted in Fig. 4, both helices C and D show a quite large angular fluctuation around an axis perpendicular to the helix axis. This fluctuation occurs for both configurations and corresponds to a maximum angular displacement of ~9°. The same essential dynamics analysis has been carried out in deoxy Ngb. The results, reported in Fig. 5 (*bottom panel*), show that a single sharp band is observed, whose position is close to the one observed for the NgbCO. The increased stiffness is likely to derive from the distal His^{64}(E7) coordination to the heme iron. The clearcut change in conformation of the CD loop is an interesting feature that may be relevant to the putative role of Ngb in controlling a $G_{\alpha\beta\gamma}$-protein transduction pathway (26), given that the mutant Glu^{53}(D3) to Gln has lost this function (27). An upward motion of the CD loop upon ligand binding has been previously reported for other globins (46). Although the direction is comparable to that observed in the present simulation, the amount of motion in Ngb is much larger.

Similarly to Mb, Ngb shows the presence of several internal cavities. In Mb, their function has been actively investigated by time-resolved spectroscopy, Laue diffraction and by MD simulations (21,23–25,47), which showed that the photolyzed CO migrates in between these cavities. Fig. 6 shows the cavities as calculated for the unliganded metNgb (Fig. 6 *A*) and the NgbCO (Fig. 6 *B*) from the crystallographic coordinates. The calculations show that the large (~247 $Å^3$) internal tunnel so peculiar to metNgb (3,4) is reshaped after CO binding: the branch at the proximal heme side is occupied by the heme and the large cavity extends on the distal side, in agreement with crystallography (12), although calculations suggest that CO binding is associated to an increase of its total volume to ~327 $Å^3$. These results are in agreement with those reported in previous x-ray studies (12) (287 $Å^3$ and 306 $Å^3$, respectively); we tend to believe that the small differences between experiments and simulations may have to be ascribed to the different package setups used for the analysis. The cavity on the distal side, corresponding to the Xe4 site in sperm whale Mb (48), is not appreciably modified (Fig. 6, *A* and *B*). In both crystal structures we calculated a second minor gap near the large cavity, which topologically corresponds to the so-called phantom1 cavity (Ph1), detected in sperm whale Mb by MD simulations (21,22). Moreover we notice that in the metNgb crystal structure (Fig. 6 *A*), the Xe2 cavity is connected to the

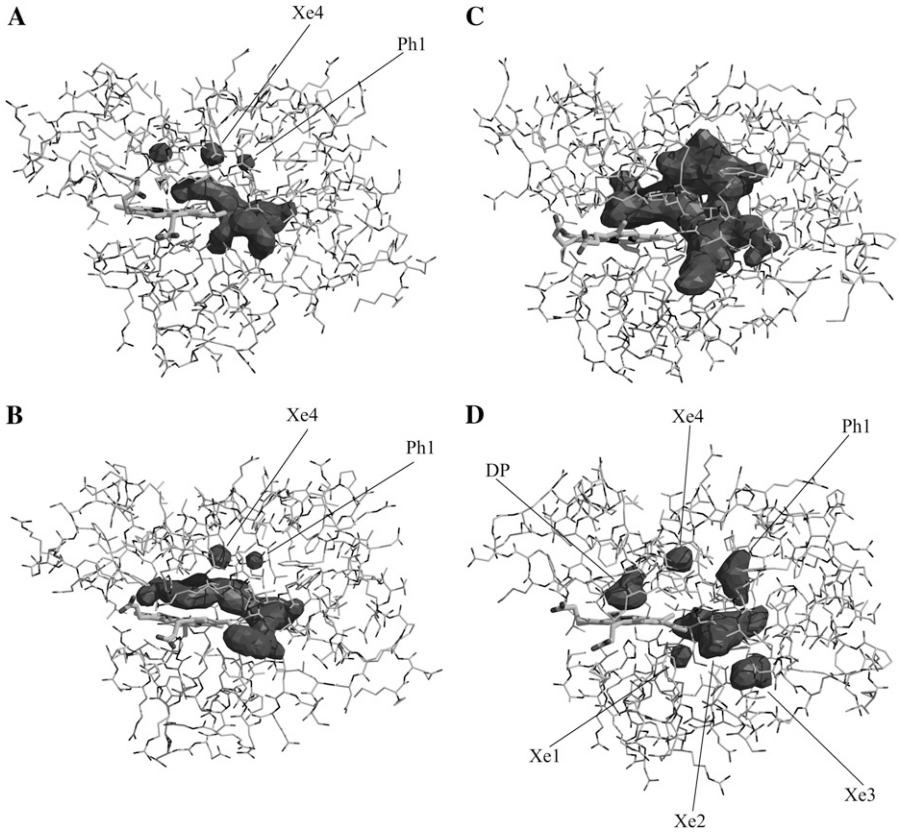

FIGURE 6 Main cavities in unliganded metNgb (*A*) and carboxy Ngb (*B*) crystal structures, detected by the package SURFNET (43). Main cavities in carboxy Ngb as detected from molecular dynamics simulation: two sample configurations, in which the cavities are fully connected (*C*) or separated (*D*) are reported. Xe1 is delimited by Leu^{92}(F4), His^{96}(F8), Phe^{106}(G5), and Met^{144}(H9), Xe3 by Ala^{75}(E8), Leu^{136}(H11), and Val^{140}(H15), while Xe4 is surrounded by Gly^{24}(B6), Leu^{27}(B9), Phe^{28}(B10), Ile^{65}(E8), Val^{68}(E11), and Met^{69}(E12). The central large cavity Xe2 is delimited by Ile^{72}(E5), Tyr^{137}(H12), and Val^{140}(H15) side chains. Finally the Ph1 cavity is delimited by Trp^{13}(A12), Leu^{113}(G12), Met^{116}(G15), Leu^{117}(G16), and Trp^{133}(H7).

Xe1 and Xe3; in NgbCO, the Xe2 cavity includes also the distal pocket (Fig. 6 *B*).

In the MD simulations of Ngb, these cavities fluctuate considerably with a behavior comparable to that observed for Mb (21,22). A snapshot from the NgbCO simulation, showing a large coalescence among the different cavities, is depicted in Fig. 6 *C*. Conversely, when the cavities are well separated, they are more similar to those identified in Mb as reported in Fig. 6 *D* (see the correspondence to the Xe1, Xe2, Xe3, Xe4, and Ph1 cavities of Mb). These cavities are coated principally by hydrophobic side chains (see Fig. 6 legend), from residues topologically corresponding to those delimiting the Xe cavities in sperm whale Mb (49); we notice that they are highly conserved in Ngb over a wide range of species. Furthermore, residues such as Trp^{13}(A12), Gly^{24}(B6), Val^{68}(E11), Leu^{92}(F4), and Leu^{117}(G16) are conserved in murine and human Mb, Hb (α and β units) and Cytgb, and also in other Mbs.

CONCLUSIONS

We have reported the results of extended (90 ns) MD simulations of deoxy and carboxy murine Ngb in water, and compared the results to the experimental x-ray data (4,12) and to the previously reported simulations of sperm whale Mb (21,22).

In the deoxy Ngb simulation, the heme position corresponds to the one observed in the metNgb crystal structure (4). On the other hand, in NgbCO the heme rapidly fluctuates between two positions that roughly correspond to the metNgb and the NgbCO crystal structures (Fig. 1 *A*). It has to be noted that the former position is not allowed in the NgbCO crystal structure, due to close contacts that would occur between bound CO and the distal His^{64}(E7); however, the simulation indicates that small displacements of His^{64}(E7) side chain drastically reduce atomic hindrance. Therefore our data show that the fairly large repositioning of the whole heme associated to CO binding to deoxy Ngb is a surprisingly fast process, occurring within the time window of the 90 ns MD simulation (Fig. 3).

According to the PMF calculation, the free energy difference between the two conformers is ~5 kJ/mol, apparently with no free energy barrier in between (Fig. 1 *B*). In the NgbCO simulation, the distal His^{64}(E7) populates two different conformations (Fig. 3) that correspond to two different χ_1 torsion angle values; these values happen to be the same observed in Mb simulations and found to correspond to the opening and closure of the so-called histidine gate (44). However, the dynamical behavior of the distal His^{64}(E7) neighbor is quite different in the two proteins. In Mb, the distal His^{64}(E7) rotation is the crucial event causing the opening and closure of the histidine gate, which has been correlated to the ligand entry and escape (50). On the other hand, in Ngb this conformational transition is associated to a substantial downward displacement of α-helix E, while no correlation is observed with the heme position (Fig. 1 *A*).

More interesting is the finding that in Ngb the configuration of the His^{64}(E7) χ_1 torsion angle is correlated to the dynamical behavior of the CD corner (Fig. 5), composed by the α-helices C and D and the CD loop. When the distal His^{64}(E7) is in the closed conformation, the CD corner populates a configuration that roughly corresponds to that observed in the metNgb crystal structure; conversely, when the distal His^{64}(E7) flips to the open conformation, the CD loop configuration is characterized by a bimodal distribution (Fig. 5). It may be of great significance to the interpretation of the physiological role of Ngb that Glu^{53}(D3) in the CD corner seems to play an essential role in the GDI function of this protein since mutation to Gln^{53}(D3) abolishes this role (27).

As reported for Mb, also in Ngb several internal cavities have been observed by crystallography. In metNgb crystal structure a very large tunnel (~300 $Å^3$), overlapping the Xe1, Xe2, and Xe3 cavities reported in Mb (48), is observed (3,4); in addition two smaller cavities, almost corresponding to the Xe4 (48) and Ph1 (21,22) cavities in Mb, are detected. Upon CO binding, the sliding motion of the heme is associated to reshaping of the large cavity, which (according to our MD simulations) slightly increases its volume extending to the distal pocket. The simulations show that these cavities fluctuate considerably, which is similar to the behavior observed in sperm whale Mb (21,22). In some frames, frequent connections between different cavities, as well as connectivity with the solvent, are observed (Fig. 6 *C*); conversely, when the cavities are well separated, they show a much more obvious correspondence to the Xe1, Xe2, Xe3, Xe4, and Ph1 cavities of Mb (Fig. 6 *D*). This observation helps in appreciating that the observed large tunnel so peculiar to Ngb is somehow an evolution and amplification of the set of cavities detected in the Mbs. Thus it may be suggested that the web of internal cavities present in the globins all share a common origin, although some clearcut variations are seen in their individual volumes. Given that Ngb is a very ancient protein (which is highly conserved among vertebrates) (2), it is a challenge to unveil the mechanistic significance of the large tunnel and its fluctuations for the physiological role of Ngb. Structural data, including crystallographic information and MD simulations, suggest that a likely role of this tunnel is to provide a space available to accommodate the heme upon the ligand-linked sliding motion (12). Whether these conformational changes are involved in modulating the in vivo function of Ngb remains to be established. Nevertheless, the correlation between the conformational change of the CD corner and the χ_1 torsion angle of His^{64}(E7) appear consistent with the hypothesis that this is a crucial event in controlling the GDI activity of Ngb and thereby its neuroprotective role, via the $G_{\alpha\beta\gamma}$ signal transduction pathway (26,27).

This work was partially supported by grants from Ministero dell'Istruzione, dell'Università e della Ricerca (Progetto di Ricerca di Rilevante Interesse Nazionale 2005 on ''Structure and Dynamics of Redox Proteins'' to A.D.N. and M.B.).

REFERENCES

1. Antonini, E., and M. Brunori. 1971. Hemoglobin and Myoglobin in Their Reactions with Ligands. North-Holland, Amsterdam.
2. Burmester, T., B. Weich, S. Reinhardt, and T. Hankeln. 2000. A vertebrate globin expressed in the brain. *Nature*. 407:520–523.
3. Pesce, A., S. Dewilde, M. Nardini, L. Moens, P. Ascenzi, T. Hankeln, T. Burmester, and M. Bolognesi. 2003. Human brain neuroglobin structure reveals a distinct mode of controlling oxygen affinity. *Structure*. 11:1087–1095.
4. Vallone, B., K. Nienhaus, M. Brunori, and G. U. Nienhaus. 2004. The structure of murine neuroglobin: novel pathways for ligand migration and binding. *Proteins*. 56:85–92.
5. Dewilde, S., L. Kiger, T. Burmester, T. Hankeln, V. Baudin-Creuza, T. Aerts, M. C. Marden, R. Caubergs, and L. Moens. 2001. Biochemical characterization and ligand binding properties of neuroglobin, a novel member of the globin family. *J. Biol. Chem.* 276: 38949–38955.
6. Nienhaus, K., J. M. Kriegl, and G. U. Nienhaus. 2004. Structural dynamics in the active site of murine neuroglobin and its effects on ligand binding. *J. Biol. Chem.* 279:22944–22952.
7. Trent III, J. T., R. A. Watts, and M. S. Hargrove. 2001. Human neuroglobin, a hexacoordinate hemoglobin that reversibly binds oxygen. *J. Biol. Chem.* 276:30106–30110.
8. Kriegl, J. M., A. J. Bhattacharyya, K. Nienhaus, P. Deng, O. Minkow, and G. U. Nienhaus. 2002. Ligand binding and protein dynamics in neuroglobin. *Proc. Natl. Acad. Sci. USA*. 99:7992–7997.
9. Van Doorslaer, S., S. Dewilde, L. Kiger, S. V. Nistor, E. Goovaerts, M. C. Marden, and L. Moens. 2003. Nitric oxide binding properties of neuroglobin. A characterization by EPR and flash photolysis. *J. Biol. Chem.* 278:4919–4925.
10. Brunori, M., A. Giuffre, K. Nienhaus, G. U. Nienhaus, F. M. Scandurra, and B. Vallone. 2005. Neuroglobin, nitric oxide, and oxygen: functional pathways and conformational changes. *Proc. Natl. Acad. Sci. USA*. 102: 8483–8488.
11. Brunori, M., and B. Vallone. 2006. A globin for the brain. *FASEB J.* 20:2192–2197.
12. Vallone, B., K. Nienhaus, A. Matthes, M. Brunori, and G. U. Nienhaus. 2004. The structure of carbonmonoxy neuroglobin reveals a heme-sliding mechanism for control of ligand affinity. *Proc. Natl. Acad. Sci. USA*. 101:17351–17356.
13. Sun, Y., K. Jin, X. O. Mao, Y. Zhu, and D. A. Greenberg. 2001. Neuroglobin is up-regulated by and protects neurons from hypoxic-ischemic injury. *Proc. Natl. Acad. Sci. USA*. 98:15306–15311.
14. Sun, Y., K. Jin, A. Peel, X. O. Mao, L. Xie, and D. A. Greenberg. 2003. Neuroglobin protects the brain from experimental stroke in vivo. *Proc. Natl. Acad. Sci. USA*. 100:3497–3500.
15. Elber, R., and M. Karplus. 1990. Enhanced sampling in molecular dynamics: use of the time-dependent Hartree approximation for a simulation of carbon monoxide diffusion through myoglobin. *J. Am. Chem. Soc.* 112:9161–9175.
16. Straub, J. E., and M. Karplus. 1991. Molecular dynamics study of the photodissociation of carbon monoxide from myoglobin: ligand dynamics in the first 10 ps. *Chem. Phys.* 158:221–248.
17. Vitkup, D., G. A. Petsko, and M. Karplus. 1997. A comparison between molecular dynamics and x-ray results for dissociated CO in myoglobin. *Nat. Struct. Biol.* 4:202–208.
18. Meller, J., and R. Elber. 1998. Computer simulations of carbon monoxide photodissociation in myoglobin: structural interpretation of the B states. *Biophys. J.* 74:789–802.
19. Shibayama, N., T. Yonetani, R. M. Regan, and Q. H. Gibson. 1995. Mechanism of ligand binding to Ni(II)-Fe(II) hybrid hemoglobins. *Biochemistry.* 34:14658–14667.
20. Mouawad, L., D. Perahia, C. H. Robert, and C. Guilbert. 2002. New insights into the allosteric mechanism of human hemoglobin from molecular dynamics simulations. *Biophys. J.* 82:3224–3245.
21. Bossa, C., M. Anselmi, D. Roccatano, A. Amadei, B. Vallone, M. Brunori, and A. Di Nola. 2004. Extended molecular dynamics simulation of the carbon monoxide migration in sperm whale myoglobin. *Biophys. J.* 86:3855–3862.
22. Bossa, C., A. Amadei, I. Daidone, M. Anselmi, B. Vallone, M. Brunori, and A. Di Nola. 2005. Molecular dynamics simulation of sperm whale myoglobin: effects of mutations and trapped CO on the structure and dynamics of cavities. *Biophys. J.* 89:465–474.
23. Bourgeois, D., B. Vallone, F. Schotte, A. Arcovito, A. E. Miele, G. Sciara, M. Wulff, P. Anfinrud, and M. Brunori. 2003. Complex landscape of protein structural dynamics unveiled by nanosecond Laue crystallography. *Proc. Natl. Acad. Sci. USA*. 100:8704–8709.
24. Srajer, V., Z. Ren, T. Y. Teng, M. Schmidt, T. Ursby, D. Bourgeois, C. Pradervand, W. Schildkamp, M. Wulff, and K. Moffat. 2001. Protein conformational relaxation and ligand migration in myoglobin: a nanosecond to millisecond molecular movie from time-resolved Laue x-ray diffraction. *Biochemistry.* 40:13802–13815.
25. Schotte, F., M. Lim, T. A. Jackson, A. V. Smirnov, J. Soman, J. S. Olson, G. N. Phillips, Jr., M. Wulff, and P. A. Anfinrud. 2003. Watching a protein as it functions with 150-ps time-resolved x-ray crystallography. *Science*. 300:1944–1947.
26. Wakasugi, K., T. Nakano, and I. Morishima. 2003. Oxidized human neuroglobin acts as a heterotrimeric G-α protein guanine nucleotide dissociation inhibitor. *J. Biol. Chem.* 278:36505–36512.
27. Wakasugi, K., and I. Morishima. 2005. Identification of residues in human neuroglobin crucial for guanine nucleotide dissociation inhibitor activity. *Biochemistry.* 44:2943–2948.
28. Du, W., R. Syvitski, S. Dewilde, L. Moens, and G. N. La Mar. 2003. Solution ^{1}H NMR characterization of equilibrium heme orientational disorder with functional consequences in mouse neuroglobin. *J. Am. Chem. Soc.* 125:8080–8081.
29. Becke, A. D. 1993. Density-functional thermochemistry. III. The role of exact exchange. *J. Chem. Phys.* 98:5648–5652.
30. Lee, C., W. Yang, and R. G. Parr. 1988. Development of the Colle-Salvetti correlation-energy formula into a functional of the electron density. *Phys. Rev. B*. 37:785–789.
31. Schmidt, M. W., K. K. Baldridge, J. A. Boatz, S. T. Elbert, M. S. Gordon, J. H. Jensen, S. Koseki, N. Matsunaga, K. A. Nguyen, T. L.Windus, and S. T. Elbert. 1993. General atomic and molecular electronic structure system. *J. Comput. Chem.* 14:1347–1363.
32. Schaefer, A., H. Horn, and R. Ahlrichs. 1992. Fully optimized contracted Gaussian basis sets for atoms lithium to krypton. *J. Chem. Phys.* 97:2571–2577.
33. Berendsen, H. J. C., J. P. M. Postma, W. F. van Gunsteren, and J. Hermans. 1981. Interaction models for water in relation to protein hydration. *In* Intermolecular Forces. B. Pullman, editor. D. Reidel Publishing, Dordrecht, The Netherlands.
34. Berendsen, H. J. C., D. van der Spoel, and R. van Drunen. 1995. GROMACS: a message-passing parallel molecular dynamics implementation. *Comput. Phys. Comm.* 91:43–56.
35. van Gunsteren, W. F., S. Billeter, A. Eising, P. Hunenberger, P. Kruger, A. E. Mark, W. Scott, and I. Tironi. 1996. Biomolecular Simulations: The GROMOS96 Manual and User Guide. BIOMOS bv, Zurich, Groningen.
36. Oostenbrink, C., A. Villa, A. E. Mark, and W. F. van Gunsteren. 2004. A biomolecular force field based on the free enthalpy of hydration and solvation: the GROMOS force-field parameter sets 53A5 and 53A6. *J. Comput. Chem.* 25:1656–1676.
37. Hess, B., H. Bekker, H. J. C. Berendsen, and J. G. E. M. Fraaije. 1997. LINCS: a linear constraint solver for molecular simulations. *J. Comput. Chem.* 18:1463–1472.
38. Amadei, A., G. Chillemi, M. A. Ceruso, A. Grottesi, and A. Di Nola. 2000. Molecular dynamics simulations with constrained roto-translational motions: theoretical basis and statistical mechanical consistency. *J. Chem. Phys.* 112:9–23.
39. Evans, D. J., and G. P. Morriss. 1990. Statistical Mechanics of Nonequilibrium Liquids. Academic Press, London, UK.

40. Feenstra, K. A., B. Hess, and H. J. C. Berendsen. 1999. Improving efficiency of large time-scale molecular dynamics simulations of hydrogen-rich systems. *J. Comput. Chem.* 20:786–798.

41. Essmann, U., L. Perera, M. L. Berkowitz, T. Darden, H. Lee, and L. G. Pedersen. 1995. A smooth particle mesh Ewald method. *J. Chem. Phys.* 103:8577–8593.

42. Amadei, A., A. B. Linssen, and H. J. Berendsen. 1993. Essential dynamics of proteins. *Proteins.* 17:412–425.

43. Laskowski, R. A. 1995. SURFNET: a program for visualizing molecular surfaces, cavities, and intermolecular interactions. *J. Mol. Graph.* 13:323–330.

44. Perutz, M. F., and F. S. Mathews. 1966. An x-ray study of azide methemoglobin. *J. Mol. Biol.* 21:199–202.

45. Beveridge, D. L., and F. M. Di Capua. 1989. Free energy via molecular simulation: a primer. *In* Computer Simulation of Biomolecular Systems. W. F. Van Gunsteren and P. K. Weiner, editors. ESCOM, Leiden, The Netherlands.

46. Guallar, V., A. A. Jarzecki, R. A. Friesner, and T. G. Spiro. 2006. Modeling of ligation-induced helix/loop displacements in myoglobin: toward an understanding of hemoglobin allostery. *J. Am. Chem. Soc.* 128:5427–5435.

47. Bourgeois, D., B. Vallone, A. Arcovito, G. Sciara, F. Schotte, P. A. Anfinrud, and M. Brunori. 2006. Extended subnanosecond structural dynamics of myoglobin revealed by Laue crystallography. *Proc. Natl. Acad. Sci. USA.* 103:4924–4929.

48. Tilton, R. F., Jr., I. D. Kuntz, Jr., and G. A. Petsko. 1984. Cavities in proteins: structure of a metmyoglobin-xenon complex solved to 1.9 A. *Biochemistry.* 23:2849–2857.

49. Frauenfelder, H., B. H. McMahon, R. H. Austin, K. Chu, and J. T. Groves. 2001. The role of structure, energy landscape, dynamics, and allostery in the enzymatic function of myoglobin. *Proc. Natl. Acad. Sci. USA.* 98:2370–2374.

50. Scott, E. E., Q. H. Gibson, and J. S. Olson. 2001. Mapping the pathways for O_2 entry into and exit from myoglobin. *J. Biol. Chem.* 276:5177–5188.